2011-09-19

Microstructure Evolution in 304L Stainless Steel Subjected to Hot Torsion at Elevated Temperature

Jian Lu
Brigham Young University - Provo

Microstructure Evolution in 304L Stainless Steel Subjected to Hot Torsion at Elevated Temperature

Jian Lu

A thesis submitted to the faculty of
Brigham Young University
in partial fulfillment of the requirements for the degree of

Master of Science

Tracy W. Nelson, Chair
Carl D. Sorensen
Michael P. Miles

Department of Mechanical Engineering

Brigham Young University

December 2011

ABSTRACT

Microstructure Evolution in 304L Stainless Steel
Subjected to Hot Torsion at Elevated
Temperature

Jian Lu
Department of Mechanical Engineering, BYU
Master of Science

The current study focus on investigating a relationship between processing variables and microstructure evolution mechanism in 304L stainless steel subjected to hot torsion. The Gleeble 3800 with Mobile Torsion Unit (MTU) is utilized in the current study to conduct hot torsion test of 304L stainless steel. Samples are rotated at 1100℃ in the shear strain rate range of $0.02s^{-1}$ to $4.70s^{-1}$ and the shear strain range of 0.5 to 4. Orientation imaging microscopy (OIM) technique is used to collect and analyze the microstructure. At low strains (≤1) and strain rate ($0.02s^{-1}$), average grain size remains relatively constant, but the lengths of DSs and LABs increase within grains. These are characteristics of the dynamic recovery (DRV). With increasing strain and strain rate, the lengths of DSs, LABs and HABs increase, accompanied by the decrease of average grain size. Subgrains with HAB segments are observed. These are characteristics of continuous dynamic recrystallization (CDRX). At strain rates greater than or equal to $0.94s^{-1}$, the fraction of deformation texture is about 3 times higher than that of rotated cube texture. The average grain size increases relative to that at a strain rate of $0.20s^{-1}$, accompanied by the increase of twin length per area. This indicates that grain growth take place after CDRX. Sigma phase is not observed in the current study due to the lack of static recrystallization (SRX) and the higher cooling rate.

Keywords: Jian Lu, friction stir welding FSW, 304L stainless steel, hot torsion, dynamic recovery DRV, continuous dynamic recrystallization CDRX, dislocation structures DSs, low angle boundaries LABs, high angle boundaries HABs

ACKNOWLEDGMENTS

The success of this research is contributed to many important people in my life. First, I would like to thank Dr. Tracy W. Nelson, Dr. Carl D. Sorensen, and Dr. Michael P. Miles, who provided valuable suggestions and feedback to my work. Also, a special thanks to my extremely kind and patient advisor, Dr. Tracy W. Nelson, who gave me the opportunity to work as his research assistant in Brigham Young University. I am grateful for my loving parents who always believe in my ability and support my decisions. Likewise, I would like to thank my life-time friend, Jingou Yin, who inspired me to continue my education in the U.S., for his continuous support and encouragement. Finally, I gratefully acknowledge the financial support of the Office of Naval Research, contract Number. N00014-09-1-0970, under the guidance of Dr. William Mullins.

TABLE OF CONTENTS

LIST OF FIGURES

1 INTRODUCTION

Friction stir welding (FSW) is a relatively new solid-joining technique [1]. Compared with traditional fusion welding techniques, FSW can be carried out with low defect density, low cost, good welding appearance, low environment impact and good mechanical/microstructural properties. Therefore, in the last decades, FSW has made rapid progress in research and industrial applications.

1.1 FSW Microstructure Evolution in Nonferrous Metal

Initially, FSW research focused on microstructure evolution research of metals with low softening temperature, such as Al, Cu and their alloys [2-6]. This was partly due to the lack of available FSW stirring tool for high softening temperature metals.

Sakthivel et al. [2] investigated the microstructure of FSW in copper. They observed fine equiaxed grains in the stir zone (SZ), elongated grains in the thermo-mechanically affected zone (TMAZ), and coarse grains in the heat-affected zone (HAZ), respectively.

Su et al. [3] observed similar results in FSW 7050-T651 Al alloy. They anticipated that continuous dynamic recrystallization (CDRX) and dynamic recovery (DRV) occurred in SZ and TMAZ, respectively. For FSW 7075 Al alloy, however, Su et al. [4] reported multiple mechanisms including dynamic recovery (DRV), discontinuous dynamic recrystallization

(DDRX), continuous dynamic recrystallization (CDRX), and grain growth at different stages in the FSW process.

1.2 FSW Applications in Ferrous and Nickel Metals

With the development of new tooling, FSW has been successfully applied to the high softening temperature metals such as ferrous alloys, stainless steels, and Ni-base alloys [7-13].

Ozekcin et al. [7] evaluated the feasibility of FSW carbon steels X80 and L80. They reported that both steels were welded without any defects and proposed that FSW could successfully join steels with different carbon contents and processing histories.

Wei et al. [8] demonstrated that FSW is a feasible way to weld or process HSLA-65. Excellent weld quality was obtained, and relationships between FSW processing parameters such as travel speed, rotation speed, and microstructures were reported.

Sato et al. [9] reported that FSW produced sound welds in Ni-base alloy 600 using PCBN tool. Finer grain structure was obtained in SZ, and the post-welded mechanical properties were improved compared to the base metal.

1.3 FSW Microstructure Evolution in Austenitic Stainless Steels

Austenitic stainless steels form an important class of engineering materials. They are widely used in the petro-chemical and other industries applications due to their excellent corrosion resistance. However, research in FSW austenitic stainless steels is limited.

Reynolds et al. [14] reported the effect of tool rotation speed on the heat input and microstructure in FSW 304L stainless steels. At a given travel speed, they found that lower tool rotation speed lead to lower weld temperature and finer grain size in SZ due to low energy input.

Sato et al. [13] investigated microstructure evolution of FSW 304L stainless steels. They reported the weld first underwent dynamic recrystallization (DRX) due to intense hot deformation and then static recrystallization (SRX) due to subsequent heating by the tool shoulder.

Kokawa et al. [15] and Park et al. [12, 16] reported that DRX and DRV structures were observed in the SZ and TMAZ of FSW 304 stainless steels, respectively.

Saeid et al. [17, 18] investigated the microstructure evolution of FSW duplex stainless steels. They proposed that austenite refinement in the SZ might result from CDRX and SRX. They [19] also reported that the grain size in SZ decreased with increasing travel speed, which was attributed to lower heat input.

Nelson [20] investigated the microstructure evolution of FSW 304L stainless steels and found no evidence of SRX and DDRX. Instead, DRV and limited CDRX were reported to be the dominant mechanisms.

1.4 Sigma Phase in FSW Austenitic Stainless Steels

Several investigators had reported the formation of sigma phase (σ) in FSW duplex and austenitic stainless steels. Park et al. [12, 16] and Okamoto et al. [21] reported the formation of sigma phase on the advancing side of the weld in FSW 304 stainless steels. Sterling [22] also reported that most sigma phase were concentrated in the lower advancing side of FSW 304L stainless steels.

Sigma phase is an iron-chrome intermediate phase with a tetragonal structure. It is undesirable because it reduces the material's toughness and corrosion resistance. Generally, sigma phase is observed in stainless steels exposed to temperature in range of 565℃ to 980℃ for

long periods of time [23]. For example, AISI 316 austenitic stainless steels were exposed at 870℃ for 60h to obtain sigma phase [24]. The presence of sigma phase in FSW was unexpected because of the short thermo-mechanical cycle and peak temperature exceeding 1000℃ in the weld region [21, 25].

Several mechanisms have been proposed to explain the formation of sigma phase in FSW. Park et al. [16] proposed the formation mechanism of sigma phase in FSW 304 stainless steels might involve the decomposition of delta ferrite into sigma and new austenite phase. They also suggested that the high strain and recrystallization induced by FSW accelerated the decomposition of delta ferrite.

Sato et al. [26] proposed that the rapid formation of intermetallic phases (σ and χ phases) in FSW superaustenitic stainless steels resulted from precipitation from austenite. In addition, they reported that the amount of intermetallic phase in FSW superaustenitic stainless steels was significantly enhanced with increasing rotation speed. They attributed it to the slower cooling rate at the higher rotation speed, which results in longer exposure to the temperature range for the precipitation during the cooling cycle.

Sorensen et al. [32] investigated sigma phase formation during FSW of a number of Fe-Ni-Cr alloys. They proposed the most likely mechanism for the sigma phase formation during FSW was SRX.

It was reported that the deformation conditions, such as temperature [16, 21, 25], cooling rate [27-29], strain rate [26, 33-35], strain [30, 31, 33-35], and recrystallization [31-35], play an important role on the formation of sigma phase and microstructure evolution in FSW austenitic stainless steel. However, due to the deformation characteristics of FSW, it is difficult to separate

the effect of some processing variables, such as strain and temperature near the stir zone. As a result, the roles of some processing variables in FSW remained unknown.

1.5 Deformation Map of 304L Stainless Steels

Hot deformation such as rolling, extrusion, forging have been investigated and the relationships between microstructure and processing variables were established. Venugopal et al. [36-38] investigated the effect of temperature and strain rate on microstructure evolution during hot deformation of 304L stainless steels at a strain of 0.5. Based on their research, a deformation map of 304L stainless steels was developed, as shown in Fig.1-1. In the temperature range of 1000℃ to 1200℃, 304L exhibits DRX in the strain rate range of $0.01s^{-1}$ to $10s^{-1}$ and grain growth in the strain rate range of $0.001s^{-1}$ to $0.003s^{-1}$, respectively. DRV is not present at the temperature higher than 1000℃.

Deformation maps of 304L stainless steels successfully established the relationship of microstructures, strain rate, and temperature during hot deformation. However, Venugopal et al. [36-38] did not investigate the effect of different strains on microstructure evolution.

1.6 Microstructure Evolution Mechanism in Hot Torsion 304L Stainless Steels

In recent years, Gleeble hot torsion has been used to simulate FSW [25, 39]. During hot torsion FSW simulation, samples were heated to a desired temperature, rotated at a desired shear strain and shear strain rate, and then cooled at a desired cooling rate. Using this approach, the effect of any processing variable on the microstructure evolution could be independently investigated.

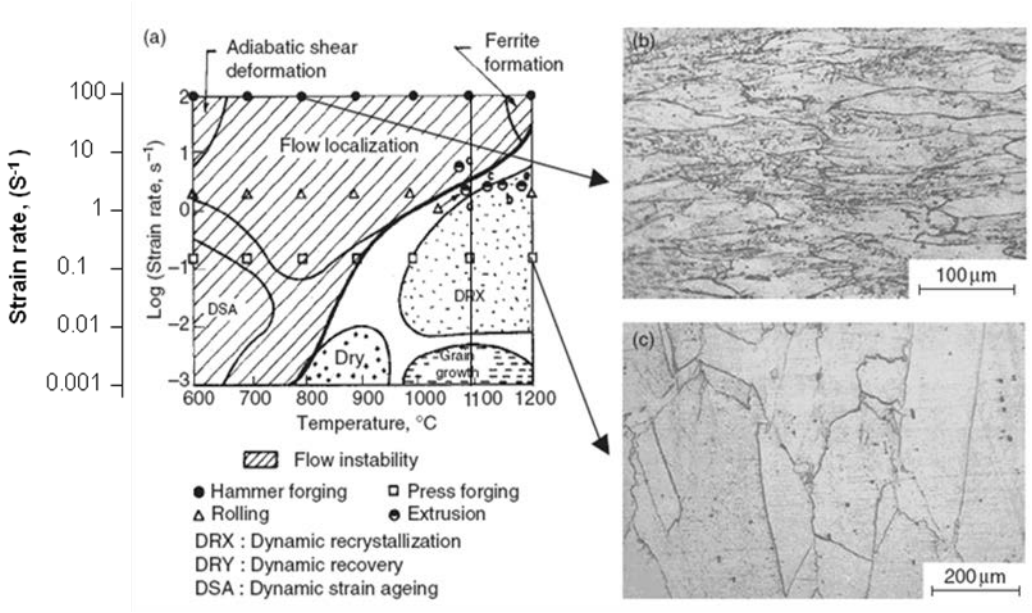

Figure 1-1 Deformation map of 304L stainless steels subjected to hot deformation and typical microstructures, a) typical deformation map of 304L stainless steels subjected to hot compression, b) Microstructure of the sample hammer deformed at 800℃ and 100s-1, c) Microstructure of the sample press forged at 1200℃ and 0.15s-1. [36]

Microstructure evolutions during hot torsion of austenitic stainless steels have been investigated, and several evolution mechanisms have been reported [3,20,34,40]. Nelson [20] reported the presence of well developed dislocation cells in hot torsion 304L at 1100℃ and considered it as evidence of DRV and possibly CDRX. On the other hand, Dehghan-Manshadi et al. [34] investigated the effect of hot torsion processing variables such as strain, strain rate, and temperature on microstructure in 304 stainless steels under a wide range of deformation temperatures (900-1100℃) and strain rates (0.01-1s^{-1}). They found that the DDRX fraction increased with increasing shear strain. Montheillet et al. [40] also reported similar results.

1.7 Objective

The objective of the current study is to investigate a relationship between processing variables and microstructure evolution in 304L stainless steel subjected to hot torsion.

Orientation imaging microscopy (OIM) technique is used to analyze the microstructure. Through the current study, an understanding of how processing variables correlate to microstructure evolution can be established. This understanding will help to determine processing variables to get desired microstructure.

2 EXPERIMENTS

2.1 Materials

A 304L austenitic stainless steel with a chemical composition of C-0.02, S-0.005, P-0.035, Ni-10.3, Cr-18.6, Mn-1.7, Si-0.58, Mo-0.07, and balance Fe, was used in the current study.

2.2 Gleeble Hot Torsion Test

The Gleeble 3800 with Mobile Torsion Unit (MTU) [41] was utilized in the current study to conduct hot torsion test of 304L stainless steel (Fig.2-1). In order to control the cooling rate, hot torsion samples modified by Norton [42], as shown in Figure 2-2, were machined and used in the current study.

Three thermocouples are welded to the torsion sample on the sample's fixed side at 0mm (0"), 6.35mm (0.25"), and 12.7mm (0.5") from the shoulder of the gauge section. The thermocouple at 12.7mm (0.5") location was used to control the heating and cooling rates.

Hot torsion tests were carried out according to the schedule illustrated in Fig.2-3. Under a rough vacuum, samples were resistively heated to 1100℃ and rotated to a given shear strain at a given shear strain rate. The specified processing window for hot torsion tests was illustrated in Fig.2-4. After torsion, the temperature of samples deceased to 200℃ at the cooling rate of roughly 9℃/s by flowing Helium cooling through the samples.

Equipment[1]: Gleeble 3800

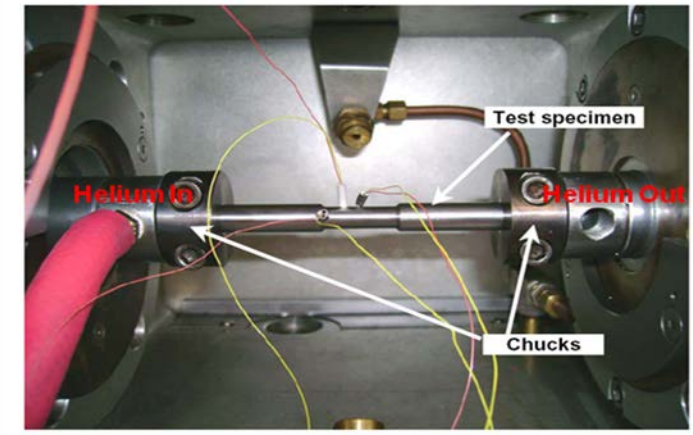

Figure 2-1 Modified Gleeble hot torsion device [41]

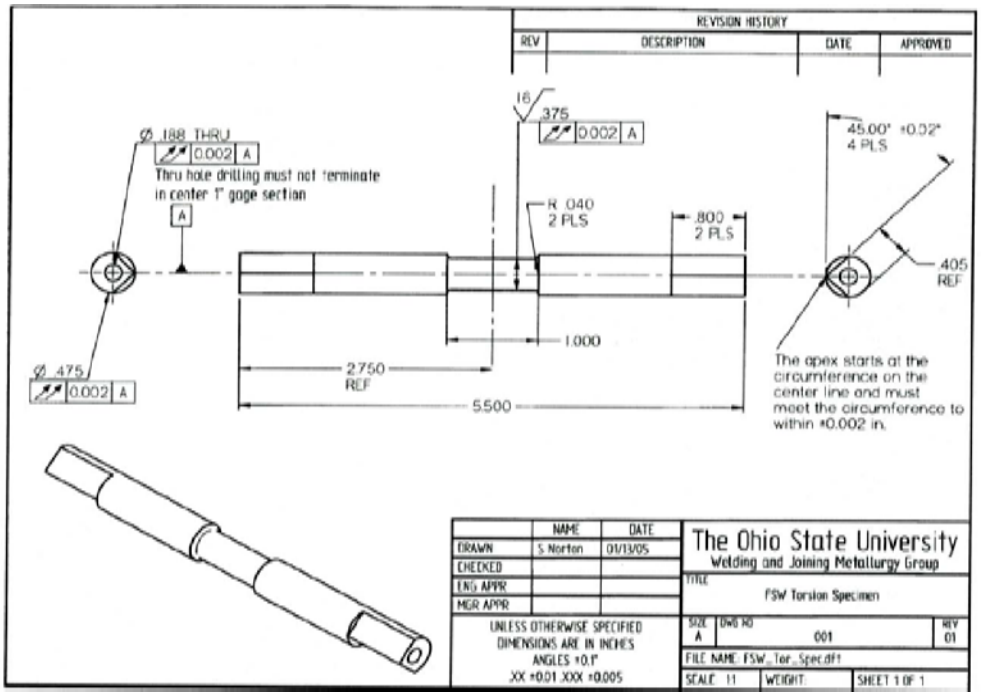

Figure 2-2 Modified Gleeble hot torsion test specimen [42]

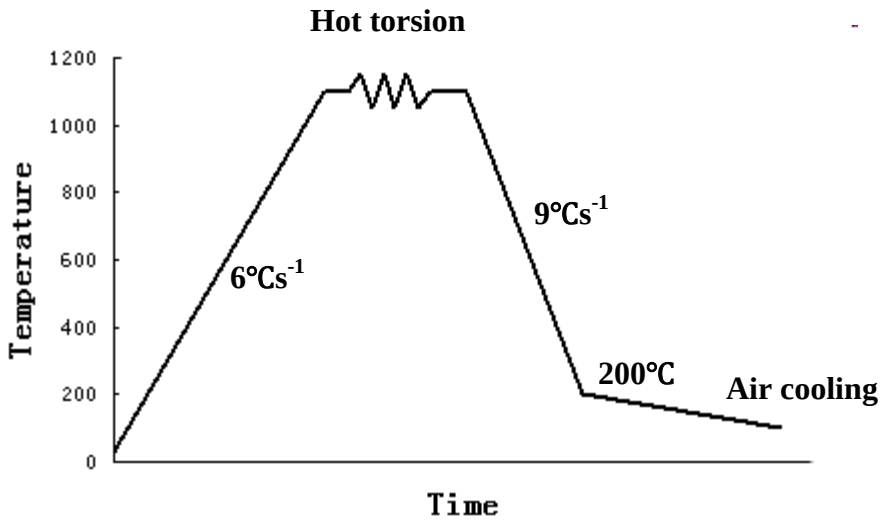

Figure 2-3 Schematic diagrams of hot torsion

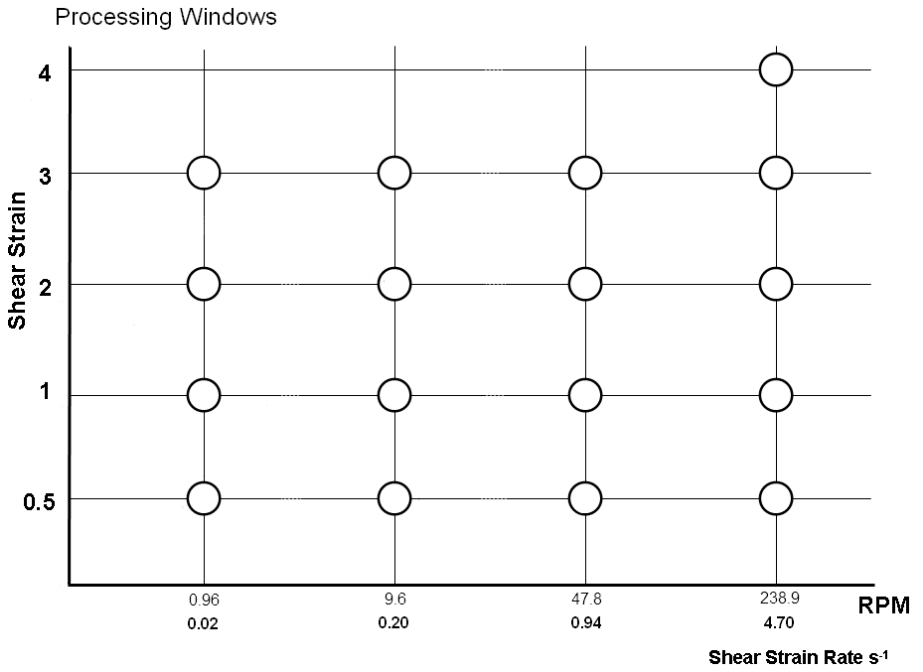

Figure 2-4 Processing windows for 304L hot torsion

For the calculation of shear strain ε and shear strain $\dot{\varepsilon}$, the following equations were used:

$$\varepsilon = {}^{r\theta}/_{L} \quad (1)$$

$$\dot{\varepsilon} = {}^{r\dot{\theta}}/_{L}, \quad \text{with } \dot{\theta} = {}^{2\pi\ RPM}/_{60} \quad (2)$$

Where r is the radius of the gauged section, L is the length of the gauged section, and θ is the angular displacement of the original line. [43].

2.3 Sample Preparation

25.4mm (1") long sections of the gauge were removed and then sectioned longitudinally by the low speed saw. All hot torsion samples were mounted and polished by 600, 1200 grit SiC grinder papers, and 9um, 6um, 3um, 1um diamond pastes on Lecloth pads. Finally, these samples were placed on a vibratory polisher with colloidal silica for 12 hours.

2.4 Instrumentation and Software for Measurement

Orientation imaging microscopy (OIM) technique was used to collect and analyze the microstructure and texture on the center of gauged section at depth of about 150um below the gauge outside surface, as shown in Fig.2-5. The OIM data were collected by a Philips XL-30 S-Feg under an accelerating voltage of 20kV and step size of 0.5um at a magnification of 800X. The OIM data were analyzed by TSL OIM Data Collection 5 software.

The microstructures, grain sizes, twin, texture, and boundary misorientation were collected and measured. The grain sizes were measured by area intercept method. Twin

boundaries were not counted as grain boundaries. The deviation of 15 degree from the ideal orientation was specified when the volume fraction of each texture component was measured.

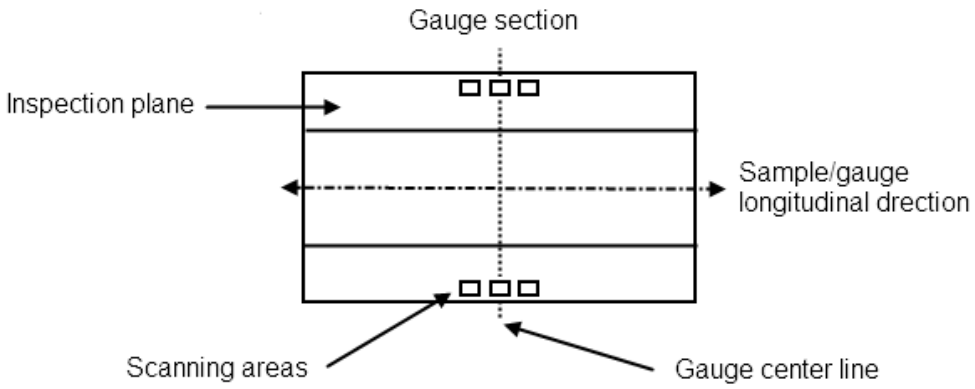

Figure 2-5 Schematic diagrams of hot torsion sample and scanning areas

3 RESULTS

3.1 General Characteristics

OIM results of the base metal and representative samples subjected to hot torsion are shown in Fig.3-1 and Fig.3-2, respectively.

The base metal microstructure (Fig.3-1) consisted of equiaxed grains with high fraction of annealing twins, which results from static recrystallization and grain growth during heat treatment [44-47]. Neither dislocation structures (DSs) nor low angle boundaries (LABs) were observed.

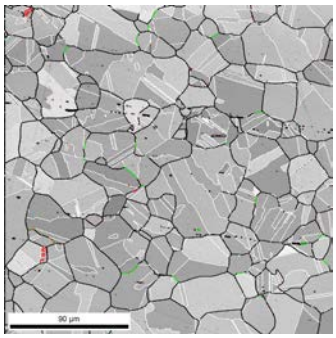

Figure 3-1 OIM grain map of the base metal, Red boundaries (DSs, 1-5° misorientation), Green boundaries (LABs, 5-15° misorientation), Black boundaries (grain boundaries, 15-180° misorientation), and White boundaries (twins)

The microstructure of samples subjected to hot torsion is shown in Fig.3-2a-l. Compared with the base metal, CB (red boundaries, below 5° misorientation) and LAB (green boundaries, 5-15° misorientation) fractions in all samples increase. Additionally, very small grains were

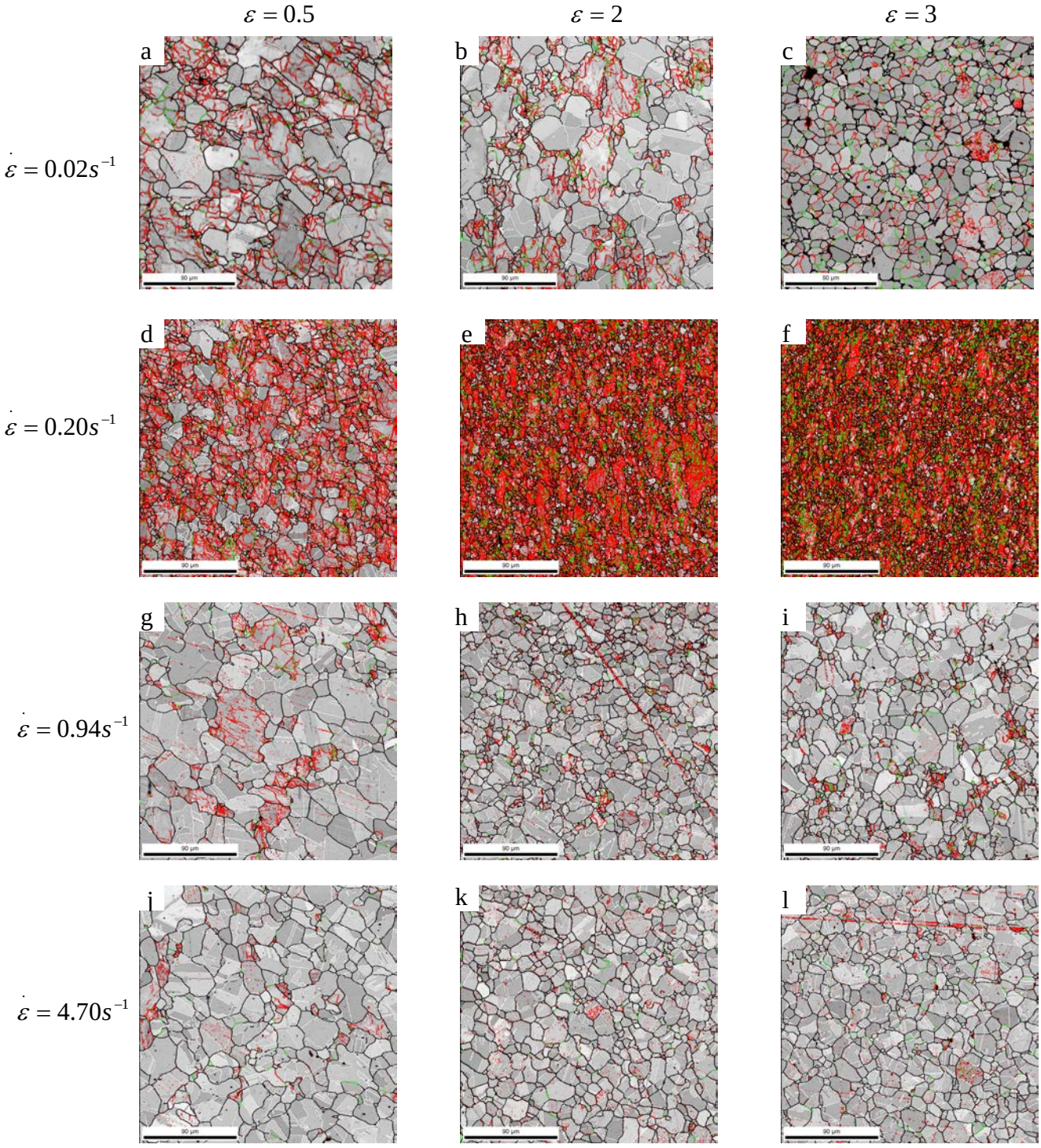

Figure 3-2 OIM grain map at the different shear strain rates and strains, a-c) shear strain rate: $0.02s^{-1}$ and strains: 0.5, 2 and 3, respectively; d-f) shear strain rate: $0.20s^{-1}$ and strains: 0.5, 2 and 3, respectively; g-i) shear strain rate: $0.94s^{-1}$ and strains: 0.5, 2 and 3, respectively; j-l) shear strain rate: $4.70s^{-1}$ and strains: 0.5, 2 and 3, respectively; Red boundaries (DSs, 1-5° misorientation), Green boundaries (LABs, 5-15° misorientation), Black boundaries (grain boundaries, 15-180° misorientation), White boundaries (twins)

generated at grain boundaries or triple junctions, and bi-modal grain size distribution was observed in most samples (Fig.3-2a, b and d-l).

3.2 Grain Size

Average grain size (grain boundary misorientation >15°) for the various shear strains and shear strain rates is shown in Fig.3-3. In general, the average grain size decreases with increasing strain and strain rate. At a strain rate of $0.20s^{-1}$, however, the average grain size is at least 30% smaller than that at other strain rates. In addition, the average grain size at low strain rate ($0.02s^{-1}$) and low strains (≤ 1) is roughly the same as that of the base metal. At high strain rates ($\geq 0.94s^{-1}$) and high strains (≥ 2), the average grain size becomes strain independent.

3.3 Lengths of DSs, LABs and HABs Per Unit Area

Lengths of DSs, LABs and HABs per unit area at the different shear strains and shear strain rates are shown in Fig.3-4. The lengths of DSs, LABs and HABs increase relative to the base metal. At a strain rate of $0.20s^{-1}$, the lengths of DSs, LABs and HABs per unit area are much higher than those at other strain rates and increase with increasing strain.

3.4 Annealing Twins

Over the range of shear strains and shear strain rates in this study, different fractions of annealing twins were observed. The twin length per unit area at different shear strains and strain rates is shown in Fig.3-5. The twin length per unit area in base metal is about $134mm^{-1}$. At strain rates below $0.94s^{-1}$, the twin length is much lower than that in the base metal. At strain rates greater than or equal to $0.94s^{-1}$, however, the twin length per unit area dramatically increases and remains high with increasing strain.

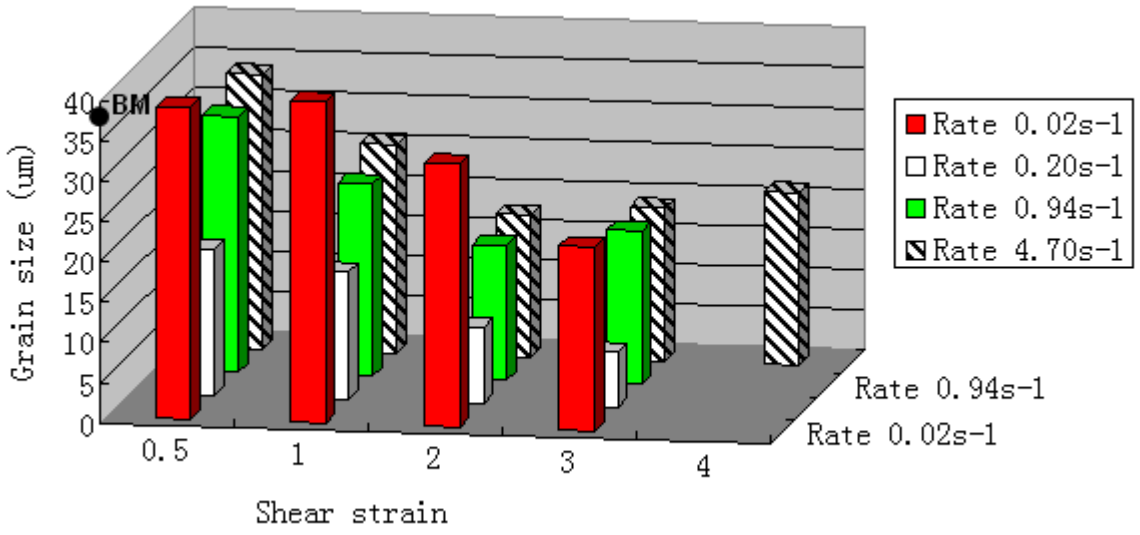

Figure 3-3 Average grain size (grain boundary misorientation >15°) at different shear strains and shear strain rates

3.5 Texture Evolution

The texture character has a close relationship with microstructure evolution [18, 20, 48-51]. Fractions of deformation texture and rotated cube textures at the different shear strains and shear strain rates are shown in Fig.3-6a) and b), respectively. The shear deformation texture in this figure consists of A, B, and C components, as reported by Nelson [20].

Fig.3-5 shows that both deformation texture and rotated cube texture are not strong. At higher strain rates ($\geq 0.94s^{-1}$), the fraction of deformation texture is about 14% higher than that of rotated cube texture. With increasing strain, the fraction of deformation texture decreases at strain rates lower than $0.94s^{-1}$, but becomes rate independent at strain rates greater than or equal to $0.94s^{-1}$.

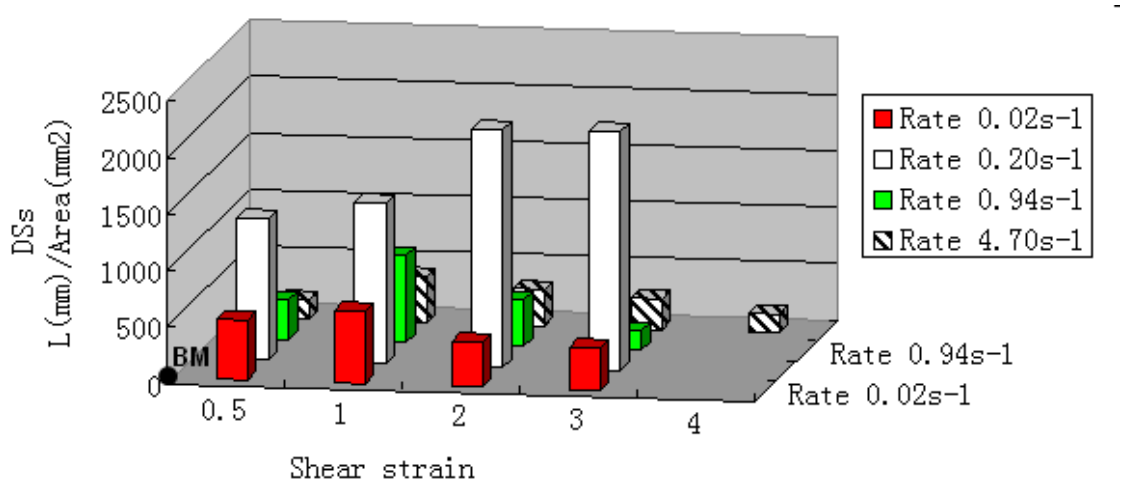

a)

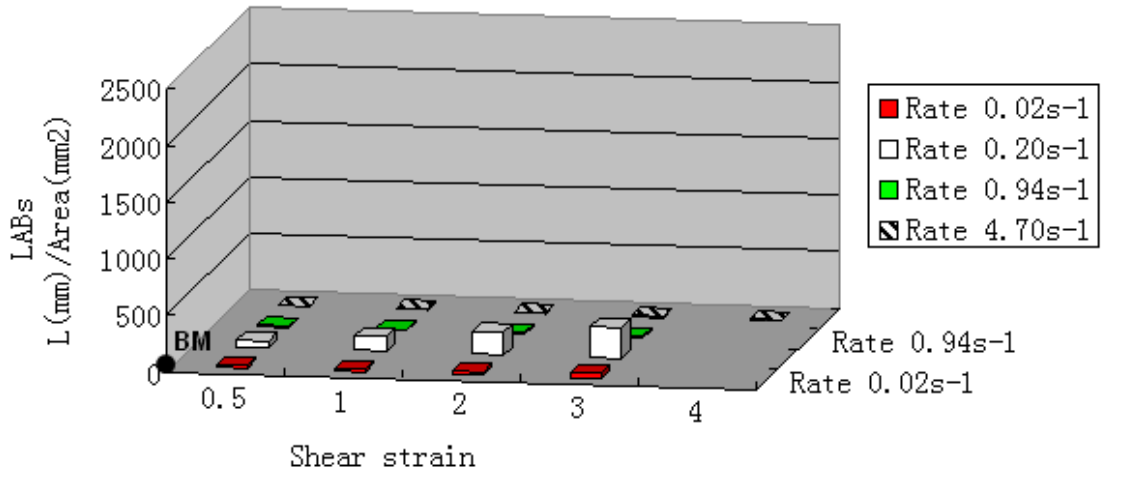

b)

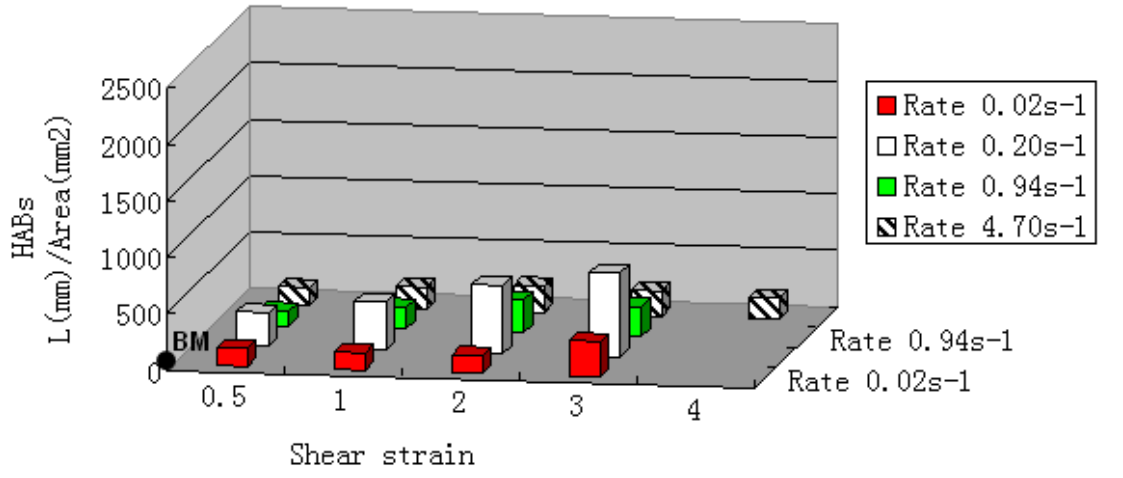

c)

Figure 3-4 Lengths of boundaries per unit area at the different shear strains and shear strain rates, a) dislocation structures (DSs), b) low angle boundary (LABs), and c) high angle boundaries (HABs)

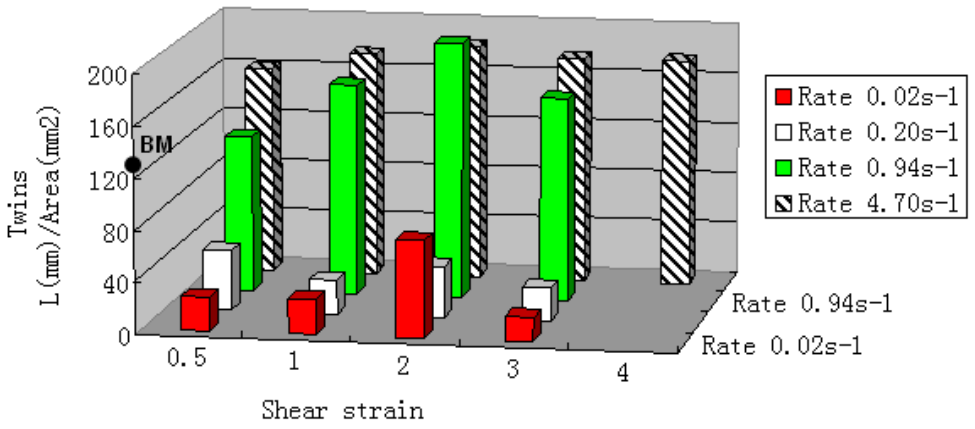

Figure 3-5 Length of twin per unit area at the different shear strains and shear strain rates

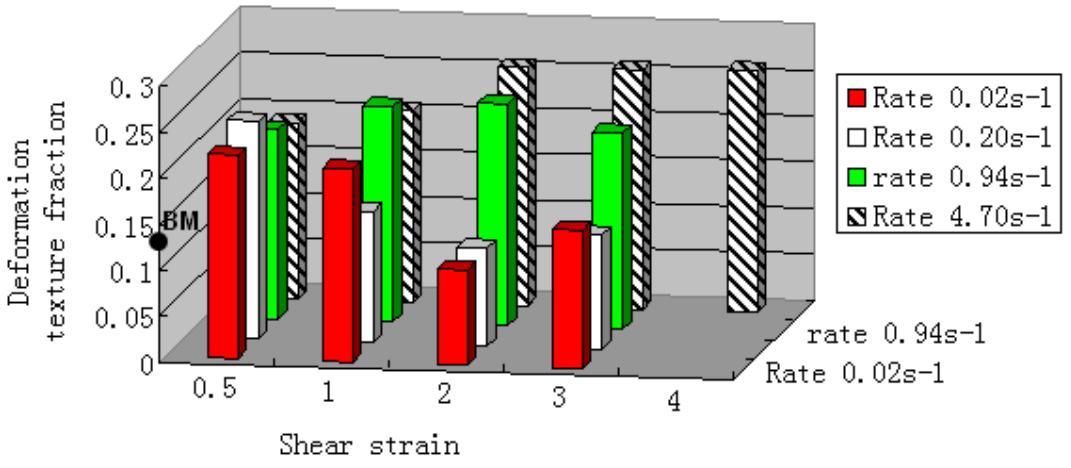

a)

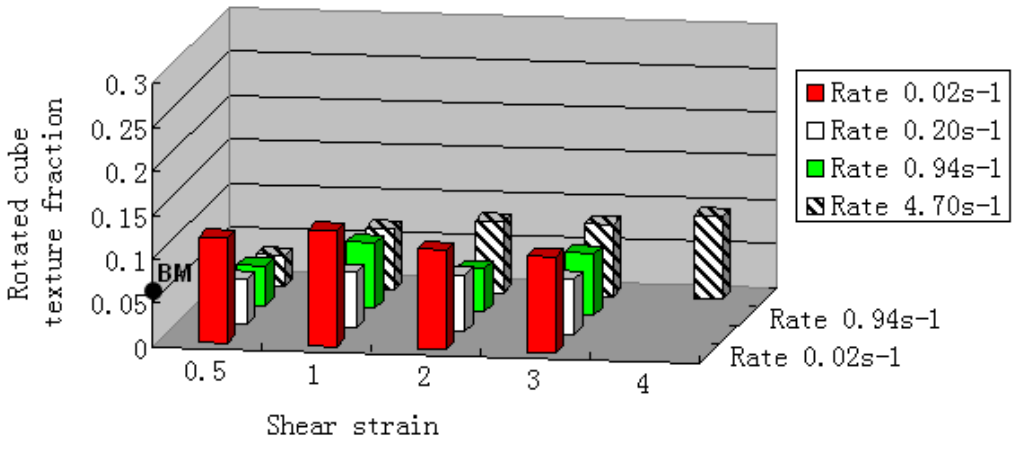

b)

Figure 3-6 Fractions of texture at the different shear strains and shear strain rates (a) deformation texture and (b) rotated cube texture

4 DISCUSSIONS

Based on the results of this investigation, a deformation map of 304L stainless steels subjected to hot torsion at 1100℃ was developed (Fig.4-1). The deformation map is broken into three regions representing different microstructure evolution mechanisms operating within those regions. The three regions are:

Region Ⅰ: at a strain rate of $0.02s^{-1}$ and strains below 2, dynamic recovery (DRV) is a dominant evolution mechanism;

Region Ⅱ: with increasing strain and strain rate, continuous dynamic recrystallization (CDRX) becomes a dominant evolution mechanism;

Region Ⅲ: at strain rates greater than or equal to $0.94s^{-1}$, grain growth (GG) takes place after CDRX;

Results of these regions will be discussed in more details.

4.1 Microstructure Evolution Mechanisms

4.1.1 Region Ⅰ

During DRV, two mechanisms are occurring: 1) dislocations are introduced by deformation; 2) dislocations climb, forming DSs and LABs or annihilating at the HABs [52].

Therefore, DRV is typically characterized by larger grains with the HABs subdivided by DSs and/or LABs. Moreover, average grain size remains nearly constant during DRV.

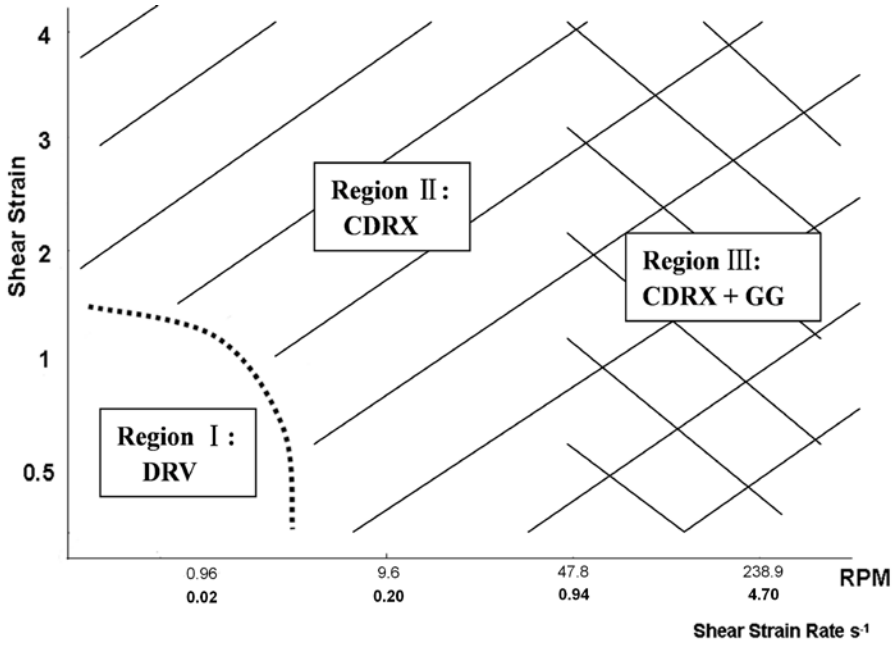

Figure 4-1 Deformation map of 304L stainless steels subjected to hot torsion at 1100℃

A typical OIM grain boundary map in region Ⅰ is shown in Fig.4-2. Clear evidences of DSs (red boundaries) and some LABs (green boundaries) within large grains were observed. Compared with the base metal, the lengths of CB and LAB per unit area in this region increase by 11 and 5 times, respectively. However, the HAB length only increases by 50% relative to the base metal (Fig.3-4). A limited number of new small grains were formed at grain boundaries, but the average grain size in this region is roughly the same as that of the base metal. These characteristics are consistent with DRV.

Although both deformation texture and rotated cube texture are weak in this region, the fraction of deformation texture in this region is about two times higher than that of rotated cube texture (Fig.3-6). This is consistent with the characteristic of DRV [20, 52-54].

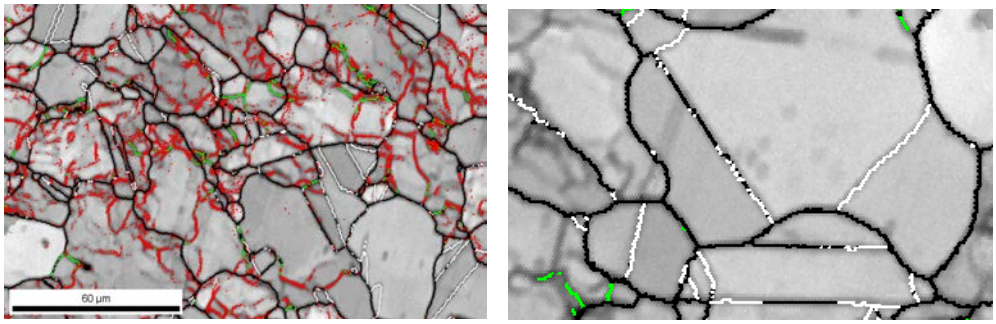

a) b)

Figure 4-2 Enlarged OIM grain boundary map for Fig.3-2a, shear strain rate: 0.02s-1 and strain: 0.5; Red boundaries (DSs, 1-5° misorientation), Green boundaries (LABs, 5-15° misorientation), Black boundaries (grain boundaries, 15-180° misorientation), White boundaries (twins)

Twin length per unit area in this region decreases by 5 times relative to the base metal (Fig.3-5). Twins were observed in a few larger grains with less cell structure (Fig.4-2). Fig.4-2b) shows that some twin boundaries (white boundaries) transferred into HABs (black boundaries). It suggests that some twin boundaries lost their characteristics during hot torsion. Beladi et al. [55] reported the similar results.

4.1.2 Region Ⅱ

CDRX involves a process of formation of LABs by DRV and progressive transformation of LABs to HABs by repeated absorption of mobile dislocations into subgrain boundaries [52]. The CDRX process has several characteristics: 1) there is no nucleation event; 2) grain boundary migration is limited; 3) DSs transform into LABs and then HABs, during which subgrains rotate. 4) Subgrain with HAB segments is a clear evidence of CDRX [56-58], 5) Smaller CDRX grains with HABs are generated, which results in the decrease of average grain size. DRX grain size generally can be predicted by theoretical calculation as follows:

$$D_{rex} = AZ^{-n}, \text{ with } Z = \dot{\varepsilon}\, exp\left(Q/_{RT}\right) \quad (3)$$

Where D_{rex} is the DRX grain size, A is a constant, Z is the Zener-Hollomon parameter, and n is the power-low exponent [59]. According to the equations (3), it can be expected that DRX grain size decreases with increasing strain rate or decreasing deformation temperature.

Comparing the different strain rates, two kinds of representative microstructure were observed in region Ⅱ. Fig.4-3. shows the OIM grain boundary map at a strain rate of $0.02s^{-1}$. Well-developed subgrains with LABs and HABs were observed. This is a clear evidence of CDRX [56-58]. Compared with samples at low strains in region Ⅰ, the length of CB per unit area decreases by about 28% in this region, but the lengths of LAB and HAB correspondingly increase (Fig.3-4), accompanied by the decrease of average grain size. This indicates that some DSs transformed into LABs and HABs. These characteristics are consistent with CDRX.

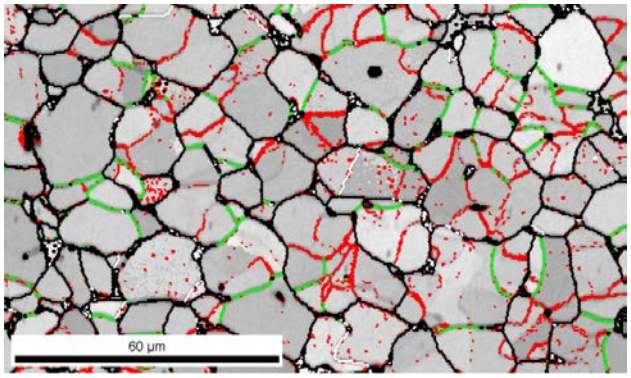

Figure 4-3 Enlarged OIM grain boundary map for Fig.3-2c, shear strain rate: 0.02s-1 and strain: 3; Red boundaries (DSs, 1-5° misorientation), Green boundaries (LABs, 5-15° misorientation), Black boundaries (grain boundaries, 15-180° misorientation), White boundaries (twins)

Fig.4-4 shows the OIM grain boundary map at a strain rate of $0.20s^{-1}$. Subgrains with HAB segments were observed in Fig.4-4b) and c), which is a typical characteristic of CDRX [56-58]. Compared with Fig.4-3, the lengths of CB, LAB, and HAB per unit area in Fig.4-4

increase by 5, 5 and 3 times (Fig.3-4), respectively. Average grain size decreases by 3 times (Fig.3-3), which is consistent with the increase of HAB length. Fig.3-4 shows that CB, LAB and HAB lengths at this strain rate increase with increasing strain. It indicates that, with increasing strain, DSs transformed into LABs and HABs. On the other hand, high dislocation density introduced by high strain rate deformation promotes CB formation by DRV.

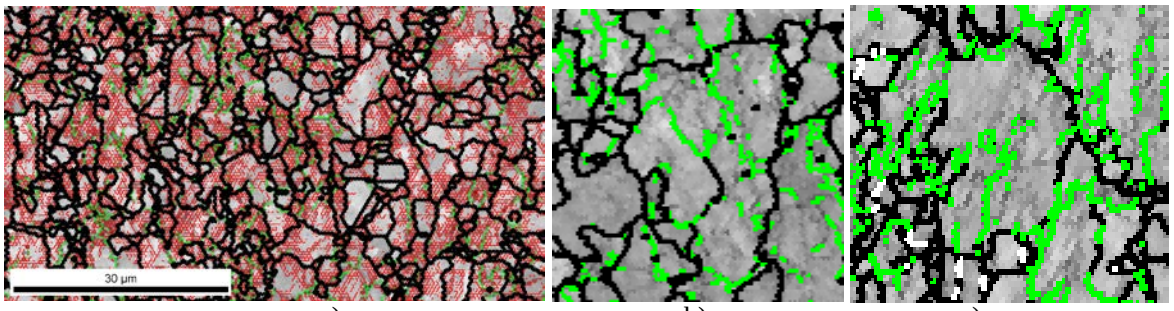

a) b) c)

Figure 4-4 Enlarged OIM grain boundary map for Fig.3-2f, shear strain rate: 0.20s-1 and strain: 3; Red boundaries (DSs, 1-5° misorientation), Green boundaries (LABs, 5-15° misorientation), Black boundaries (grain boundaries, 15-180° misorientation), White boundaries (twins)

Like samples in region Ⅰ, the twin length per unit area in region Ⅱ (Fig.4-3) is still very low (Fig.3-5). This indicates that the grain boundary migration is limited [45-47, 60, 61], which is consistent with CDRX.

It is noteworthy that the fraction of deformation texture decreases at strains greater than 1 in this region (Fig.3-6a). Hughes et al. [62] reported that the grain subdivision during deformation by boundaries such as dense dislocation walls and subgrains weakens texture. In the current study, it seems that the formation and rotation of subgrains within original large grains during CDRX weaken the deformation texture.

4.1.3 Region Ⅲ

A representative OIM grain boundary map in region Ⅲ is shown in Fig.4-5. With increasing strain rates above $0.20s^{-1}$, the CB, LAB, and HAB lengths per unit area decrease by more than 200% relative to those in region Ⅱ at a given strain (Fig.3-4).

The fraction of deformation texture in this region is about 3 times higher than that of rotated cube texture (Fig.3-6). This is consistent with the characteristic of CDRX [20, 52-54]. The deformation texture fraction in this region is higher and remains constant with increasing strain, instead of decrease like that in region Ⅱ (Fig.3-6a). It might be related to higher strain rate deformation. Bhattacharyya et al. [63, 64] proposed that increasing strain rate enhances strain hardening, which restrict grain rotations. Further study is necessary.

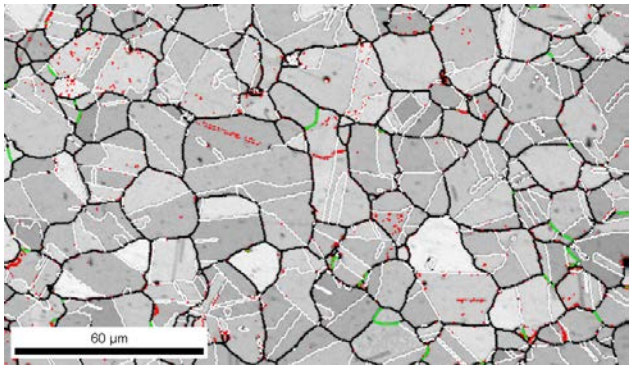

Figure 4-5 Enlarged OIM grain boundary map for Fig.3-2l, shear strain rate: 4.70s-1 and strain: 3; Red boundaries (DSs, 1-5° misorientation), Green boundaries (LABs, 5-15° misorientation), Black boundaries (grain boundaries, 15-180° misorientation), White boundaries (twins)

The average grain size in this region is more than 53% larger than that in region Ⅱ at a given strain (Fig.3-3). This is consistent with the more than 50% decrease in HAB length per unit area (Fig.3-4c). However, according to the theoretical calculation of DRX grain size (1), the DRX grain size should decrease with increasing strain rate from region Ⅱ to region Ⅲ. This

indicates that grain growth process took place after the formation of CDRX grains. This result is supported by the generation of annealing twins in this region. Compared with the twin length per area in region Ⅰ and Ⅱ, the twin length in region Ⅲ increases by more than 100% (Fig.3-5), which results from the large-scale grain boundary migration [45-47, 60, 61].

Grain growth in region Ⅲ results from the effect of higher strain rate deformation. Higher strain rate in this region introduces a large number of smaller CDRX grains according to the theoretical calculation of DRX grain size (3). These small CDRX grains decrease the distance that dislocations migrate to grain boundaries, which results in low dislocation density within CDRX grains. After matrix is replaced by new dislocation-free grains, further annealing results in grain growth. [52]

The roughly constant average grain size at strains greater than 2 in region Ⅲ (Fig.3-3) results from the effect of high strain deformation. Increasing strain enhances CDRX fraction, which decreases the average grain size. At strains greater than or equal to 2, full CDRX is reached and the average CDRX grain size no longer changes with strain, which results in the final grain size being constant.

4.2 Sigma Phase

Sigma phase, which has been reported in FSW 304 austenitic stainless steel [12, 16, 21, 22], was not observed in the current study. This results from the lack of static recrystallization (SRX) mechanism and higher cooling rate.

Lena et al. [30] investigated the effect of cold work on the formation of sigma phase in austenitic stainless steel. They reported that the formation of sigma phase correlates with recrystallization (SRX). If the amount of cold work is insufficient to produce SRX at a given temperature, the formation of sigma phase is retarded. Sorensen et al. [32] studied the formation

of phase formation in a number of FSW Fe-Ni-Cr alloys. They proposed that the most likely mechanism for the formation of sigma phase is static recrystallization (SRX). In the current study, SRX is not dominant mechanism. As a result, sigma phase was not formed.

Another possible reason is the effect of cooling rate. Sieurin et al. [27] studied the effect of cooling rate on the formation of sigma phase. They reported that, when the cooling rate exceeded the critical value $0.23 Ks^{-1}$, the formation of sigma phase could be prevented. Chen and Chiu [28, 29] reported the similar results. The cooling rate in the current study is about $9℃s^{-1}$, which is much higher than the critical value that Sieurin et al. [27] reported. Therefore, the formation of sigma phase was prohibited.

5 CONCLUSIONS

In the current study, a relationship between shear strain and strain rate, and microstructure evolution mechanism in 304L stainless steel subjected to hot torsion was investigated. The following conclusions can be made from the investigation:

- At low strains (≤1) and strain rate ($0.02s^{-1}$), DRV is a dominant mechanism. The average grain size remains relatively constant, but the lengths of DSs and LABs increase within grains.
- With increasing strain rates above $0.02s^{-1}$, or increasing strain above 1 at low strain rate ($0.02s^{-1}$), CDRX becomes a dominant mechanism. High density of dislocations is induced, which enhances the lengths of DSs, LABs and HABs, accompanied by the decrease of average grain size. Subgrains with HAB segments are observed.
- At strain rates greater than or equal to $0.94s^{-1}$, grain growth takes place after CDRX. The fraction of deformation texture is about 3 times higher than that of rotated cube texture. The average grain size increases relative to that at a strain rate of $0.20s^{-1}$, accompanied by the increase of twin length per area.
- Sigma phase is not observed in the current study. There are two possible reasons: First, no SRX, i.e., no nucleation and growth, involved in microstructure evolution process; Second, the cooling rate in the current study is much higher than the critical value for the formation of sigma phase.

6 SUGGESTIONS FOR FUTURE WORK

For future work, it is helpful to investigate the microstructure of immediately quenched samples after hot torsion. In the current study, samples were cooled at about 9℃s^{-1} from 1100℃ to 200℃ after hot torsion by flowing Helium cooling through the samples. It took about 100s, during which some microstructure evolution took place, such as grain growth in region Ⅲ. If samples are immediately quenched after hot torsion, the effect of grain growth as well as other static microstructure evolution can be eliminated, and CDRX microstructure can be preserved. As a result, the analysis of CDRX microstructure of quenched samples as well as post-deformation microstructure in the current study can improve the understanding on the whole process of microstructure evolution in 304L stainless steel during hot torsion.

Another helpful work is to investigate the microstructure of samples deformed at higher strain rates and temperature than those in the current study. In the current study, deformation temperature is 1100℃, and strain rate range is from 0.02s^{-1} to 4.70s^{-1}. i.e., 0.96-238.9 rpm (revolution per minute). Since 304L stainless steels generally carry out FSW at higher rotation speeds (300-1180 rpm) [13,14,65], and peak temperatures (1056℃-1359℃) [65,25], the microstructure investigation of 304L steel at higher strain rates and temperatures will help to improve the understanding on FSW 304L stainless steel.

REFERENCES

[1] Thomas, W.M., Nicholas, E.D., Needham, J.C., Murch, M.G., Templesmith, P., and Dawes, C.J. (1991). "Friction-stir butt welding." GB Patent No.9125978.8, *International patent application*. No. PCT/GB92/02203

[2] Sakthivel, T. and Mukhopadhyay, J. (2007). "Microstructure and Mechanical Properties of Friction Stir Welded Copper." *Journal of Material Science*, 42, 8126–8129.

[3] Su, J.Q, Nelson, T.W., Mishra, R., and Mahoney, M. (2003). "Microstructural Investigation of Friction Stir Welded 7050-T651 Aluminium." *Acta Materialia*, 51, 713–729.

[4] Su, J.Q, Nelson, T.W., and Sterling, C.J. (2005). "Microstructure Evolution during FSW/FSP of High Strength Aluminum Alloys." *Materials Science and Engineering A*, 405, 277–286.

[5] Arora, K.S., Pandey, S., Schaper, M., and Kumar, R. (2010). "Microstructure Evolution during Friction Stir Welding of Aluminum Alloy AA2219." *Journal of Materials and Technology*, 26(8), 747-753.

[6] Sato, Y.S., Urata, M., Kurihara, Y., Park, S.H.C., Kokawa, H., Ikeda, K., and Tsuji, N. (2006). "Microstructural Evolution During Friction Stir Welding of Ultrafine Grained Al alloy." *Materials Science Forum*, Vol.503-504, 169-174.

[7] Ozekcin, A., Jin, H. W., Koo, J. Y., Bangaru, N. V., and Ayer, R. (2004). "A Microstructural Study of Friction Stir Welded Joints of Carbon Steels." *International Journal of Offshore and Polar Engineering*, 14(4), 284-288.

[8] Wei, L.Y. and Nelson, T.W. (2008). "Characterization of Microstructures and Transformation Behavior in Friction Stir Welded HSLA-65." *Trends in Welding Research, Proceedings of the 8th International Conference*. 391-397.

[9] Sato, Y.S., Arkom, P., Kokawa, H., Nelson, T.W., and Steel, R.J. (2008). "Effect of microstructure on properties of friction stir welded Inconel alloy 600." *Materials Science and Engineering A*, 477, 250-258.

[10] Collier, M., Steels, R., Nelson, T., Sorensen, C., and Packer, S. (2003). "Grade development of polycrystalline cubic boron nitride for friction stir processing of ferrous alloys." *Materials Science Forum*, Vol.426-432, 3011-3016.

[11] Sorensen, C.D. and Nelson, T.W. (2007). "Friction Stir Welding of Ferrous and Nickel Alloys." *Friction Stir Welding and Processing (ASM International)*, 111-121

12] Park, S.H.C., Sato, Y. S., Kokawa, H., Okamoto, K., Hirano, S., and Inagaki, M. (2005). "Microstructures and Properties of Friction Stir Welded 304 Austenitic Stainless Steels." *Welding International*, 19(11), 877-881.

[13] Sato, Y.S., Nelson, T.W., and Sterling, C.J. (2005). "Recrystallization in Type 304L stainless steels during friction stirring." *Acta materialia*, 53, 637-645.

[14] Reynolds, A.P., Tang, W., Gnaupel-Herold, T., and Prask, H. (2003). "Structure, properties, and residual stress of 304L stainless steels friction stir welds." *Scripta Materialia*, 48, 1289–1294.

[15] Kokawa, H., Park, S.H.C., Sato, Y.S., Okamoto, K., Hirano, S., and Inagaki, M. (2008). "Microstructural evolution in 304 austenitic stainless steels during friction stir welding." *Materials Science Forum*, 580-582, 9-12.

[16] Park, S.H.C., Sato, Y.S., Kokawa, H., Okamoto, K., Hirano, S., and Inagaki, M. (2003). "Rapid formation of the sigma phase in 304 stainless steels during friction stir welding." *Scripta Materialia*, 49, 1175-1180.

[17] Saeid, T., Abdollah-zadeh, A., Shibayanagi, T., Ikeuchi, K., and Assadi, H. (2010). "EBSD Investigation of Friction Stir Welded Duplex Stainless Steels." *World Academy of Science, Engineering and Technology*, 61, 376-379.

[18] Saeid, T., Abdollah-zadeh, A., Shibayanagi, T., Ikeuchi, K., and Assadi, H. (2010). "On the formation of grain structure during friction stir welding of duplex stainless steels." *Materials Science and Engineering A*, 527, 6484–6488.

[19] Saeid, T., Abdollah-zadeh, A., Assadi, H., and Ghaini, F.M. (2008). "Effect of friction stir welding speed on the microstructure and mechanical properties of a duplex stainless steels." *Materials Science and Engineering A*, 496, 262–268.

[20] Nelson, B.D. (2010). "Using Design of Experiments and Electron Backscatter Diffraction to Model Extended Plasticity Mechanisms In Friction Stir Welded AISI 304L Stainless Steels." A thesis submitted to the faculty of Brigham Young University in partial fulfillment of the requirements for the degree of Master of Science, Department of Mechanical Engineering, Brigham Young University

[21] Okamoto, K., Hirano, S., Inagaki, M., Park, S. H. C., Sato, Y. S., Kokawa, H., Nelson, T. W., and Sorensen, C. D. (2003). "Metallurgical and mechanical properties of friction stir welded stainless steels." *4th International Symposium on Friction Stir Welding*, Utah, Abington Publishing.

[22] Sterling, C.J. (2004). "Effects of friction stir processing on the microstructure and mechanical properties of fusion welded 304L stainless steel." A thesis submitted to the faculty of Brigham Young University in partial fulfillment of the requirements for the degree of Master of Science, Department of Mechanical Engineering, Brigham Young University

[23] ASM International, (1990) "Properties and Selection: Irons, Steels, and High-performance Alloys." *ASM handbook*, Vol.1, 708-710,

[24] Shehata, M.T., Lavigne, M.J.A., and Boyd, J.D. (1983). "A quantitative metallographic study of the ferrite to sigma transformation in type 316 stainless steel." *Microstructural Science*, 11, 89-99.

[25] Sinfield, M.F. (2007). "Advancements in Physical Simulation and Thermal History Acquisition Techniques for Ferrous Alloy Friction Stir Welding." A Thesis Presented in Partial Fulfillment of the Requirements for the Degree Master of Science in the Graduate School, Ohio State University

[26] Sato, Y.S., Harayama, N., Kokawa, H., Inoue, H., Tadokoro, Y., and Tsuge, S. (2009). "Evolution of microstructure and properties in friction stir welded superaustenitic stainless steels." *Science and Technology of Welding and Joining*, 14(3), 202-209.

[27] Sieurin, H. and Sandstrom, R., (2007). "Sigma phase precipitation in duplex stainless steels 2205." *Materials Science and Engineering A*, 444, 271–276.

[28] Chen, T.H. and Yang, J.R. (2001). "Effects of solution treatment and continuous cooling on σ-phase precipitation in a 2205 duplex stainless steels." *Materials Science and Engineering A*, 311, 28–41.

[29] Chiu, L.H., Hsieh, W.C., and Wu, C.H. (2003). "Cooling rate effect vacuum brazed joint properties for 2205 duplex stainless steels." *Materials Science and Engineering A*, 354, 82–91.

[30] Lena, A.J. and Curry, W.E. (1955). "The effect of cold work and recrystallization on the formation of the sigma phase in highly stable austenitic stainless steels." *Transactions of American Society for Metals*, 47, 193-210.

[31] Singhal, L.K., Bhargava, S.N., and Martin, J.W. (1972). "The effect of plastic deformation on the formation of sigma phase in an austenitic stainless steel." *Metallography*, 5(1), 31-39.

[32] Sorensen, C.D., Nelson, T.W. (2005). "Sigma Phase Formation in Friction Stirring of Iron-nickel-Chromium Alloys. *7th International Conference on Trends in Welding Research*, 441-446, Callaway Gardens Resort, Pine Mountain, Georgia, USA

[33] Mataya, M.C., Brown, E.L., and Riendeau, M.P. (1990). "Effect of hot working on structure and strength of type 304L austenitic stainless steel." *Metallurgical transactions A*, 21A, 1969-1987.

[34] Dehghan-manshadi, A., Barnett, M.R., and Hodgson, P.D. (2008). "Hot Deformation and Recrystallization of Austenitic Stainless Steel: Part I. Dynamic Recrystallization." *Metallurgical and Materials Transactions A*, 39A, 1359-1370.

[35] Dehghan-manshadi, A., Barnett, M.R., and Hodgson, P.D. (2008). "Hot Deformation and Recrystallization of Austenitic Stainless Steel: Part Ⅱ. Post-deformation Recrystallization." *Metallurgical and Materials Transactions A*, 39A, 1371-1381.

[36] Venugopal, S., Mannan, S. L., and Prasad, Y. V. R. K. (1992). "Optimization of hot workability in stainless steels type AISI 304 L using processing maps." *Metallurgical Transactions A (USA)*, 23A, 3093-3103.

[37] Venugopal, S., Mannan, S. L., and Rodriguez, P. (2002). "Optimum design of a hot extrusion process for AISI type 304L stainless steels using a model for the evolution of microstructure." *Modelling and Simulation in Materials Science and Engineering*, 10, 253-265.

[38] Venugopal, S. and Sivaprasad, P.V. (2003). "A Journey with Prasad's Processing Maps." *Journal of Materials Engineering and Performance*, 12(6), 674-686.

[39] Failla Ⅱ, D.M. (2009). "Friction stir welding and microstructure simulation of HSLA- 65 and austenitic stainless steels." A Thesis Presented in Partial Fulfillment of the Requirements for the Degree Master of Science, Ohio State University

[40] Montheillet, F. and Thomas, J.P. (2004). "Dynamic recrystallization of low stacking fault energy metals." *Metallic Materials with High Structural Efficiency*,146, 357–368

[41] Sinfield, M.F., Lippold, J.C., and Alexandrov, B.T. (2008) "Physical simulation of friction stir weld microstructure of a high-strength, low alloy steel HSLA-65." *7th international friction stir welding symposium*, Awaji island, Japan.

[42] Norton, S.J. (2006). "Ferrous Friction Stir Weld Physical Simulation, in Welding Engineering." A Dissertation Presented in Partial Fulfillment of the Requirements for the Degree Doctor of Philosophy in the Graduate School of The Ohio State University

[43] Cao, G.H., Klöden, B., Rybacki, E., Oertel, C.G., Skrotzki, W., "High strain torsion of a TiAl-based alloy." *Materials science and engineering A*, 483-484, 512-516.

[44] Dehghan-Manshadi, A., Barnett, and M.R., Hodgsonb, P.D. (2008). "Recrystallization in AISI 304 austenitic stainless steel during and after hot deformation." *Materials Science and Engineering A*, 485, 664–672.

[45] Mahajan, S., Pande, C. S., Imam, M. A., and Rath, B. B. (1997). "Formation of annealing twins in f.c.c. crystals." *Acta Materialia*, 45(6), 2633-2638.

[46] Humphreys, F.J. and Hatherly, M. (2004). *Recrystallization and related annealing phenomena*. 261-267, Oxford: Elsevier.

[47] Rath, B.B., Imam, M.A., and Pande, C.S. (2000). "Nucleation and growth of twin interfaces in FCC metals and alloys", *Materials Physics and Mechanics*. 1, 61-66.

[48] Brown, E.L. and Deardo, A.J. (1981). "On the origin of equiaxed austenite grains that result from the hot rolling of steel." *Metallurgical* transactions A, 12A, 39-47.

[49] Klöden, B., Rybacki, E., Oertel, C.G., and Skrotzki, W. (2007). "Grain refinement and texture formation in torsion deformed NiAl." *International Journal of Materials Research*, 98(4), 276-282.

[50] Pérez-Prado, M. T. and González-Doncel, G. (1999). "Texture changes during deformation of a 7475 superplastic aluminum sheet alloy." *Textures and Microstructures*, 34, 33-42.

[51] Bocher, P., Azar, J., Adams, B.L., and Jonas, J.J. (1998). "Using OIM to Interpret the Dynamically Recrystallized Texture of a Low Stacking Fault FCC Material." *Materials Science Forum*, Vols:273-275, 249-254.

[52] "Recovery, Recrystallization, and Grain-Growth Structures." *ASM Handbook*, 14A, 552-562, Ohio: ASM International.

[53] Doherty, R.D., Hughes, D.A., Humphreys, F.J., Jonas, J.J., Jensen, D.J, Kassner, M.E., King, W.E., McNelley, T.R., McQueen, H.J., and Rollett, A.D. (1997). "Current issues in recrystallization: a review", *Materials Science and Engineering A*, 238, 219-274.

[54] "Polycrystal Modeling, Plastic Forming, and Deformation Textures." *ASM Handbook*, 14A, 671-683, Ohio: ASM International.

[55] Beladi, H., Cizek, P., and Hodgson, P.D. (2009). "Dynamic Recrystallization of Austenite in Ni-30 Pct Fe Model Alloy: Microstructure and Texture Evolution." *Metallurgical and Materials Transactions A*, 40A, 1175-1189.

[56] Du, X., Wu, B. (2005). "Continuous dynamic recrystallization of extruded NiAl polycrystals during the superplastic deformation process." *Metallurgical and Materials Transactions A*, 36A, 3343-3351.

[57] Gourdet, S., Montheillet, F. (2003). "A model of continuous dynamic recrystallization." *Acta Materialia 51*, 2685–2699.

[58] Eghbali, B. (2010). "Effect of strain rate on the microstructural development through continuous dynamic recrystallization in a microalloyed steel." *Materials science and engineering A*, 527, 3402-3406.

[59] Beer, A.G. and Barnett, M.R. (2007). "Microstructural development during hot working of Mg-3Al-1Zn." *Metallurgical and Materials Transactions A*, 38A, 1856-1867.

[60] Montheillet, F. and Coze, J.L. (2002). "Influence of purity on the dynamic recrystallization of metals and alloys." *Physica Status Solidi (A)*, 189(1), 51-58.

[61] Yamagata, H., Ohuchida, Y., Saito, N., and Otsuka, M. (2001). "Dynamic recrystallization and dynamic recovery of 99.99 mass% aluminum single crystal having [112] orientation." *Journal of materials science letters*, 20, 1947-1951.

[62] Hughes, D.A., and Hansen, N. (1993). "A comparison of the evolution of cold and hot deformation microstructures and textures in FCC metals." *Proceedings of the TMS Symposium on Advances in Hot Deformation Textures and Microstructures*, 1-18, Pittsburgh

[63] Bhattacharyya, A., Rittel, D. and Ravichandran, G. (2005). "Effect of strain rate on deformation texture in OFHC copper." *Script Materialia*, 52, 657-661.

[64] Bhattacharyya, A., Rittel, D. and Ravichandran, G. (2006). "Strain rate effect on the evolution of deformation texture for α-Fe." *Metallurgical and materials transactions A*, 37A, 1137-1145.

[65] Prasanna, P., Rao, B.S., and Rao, G.K.M., (2010). "Finite element modeling for maximum temperature in friction stir welding and its validation." *The International Journal of Advanced Manufacturing Technology*, 51, 925-933.

APPENDIX A. ROTATION OF COORDINATE SYSTEM AND TEXTURE

Since OIM analysis software is based on a rolling deformation coordinate system (RD-TD-ND system), it is necessary to rotate to a torsion simple shear deformation coordinate system (SPN-SD-XD system). In the current study, the textures were rotated 90° about TD and 90° about ND in order to analyze textures in an appropriate coordinate system. [20] The orientation Euler angles of the rotated cube texture and A, B, C components of the deformation texture are shown as follows.

A components

φ1	Φ	φ2
35.2	45	0
35.2	135	0
144.8	45	0
144.8	135	0
215.2	45	0
215.2	135	0
324.8	45	0
324.8	135	0
0	35.3	45
0	144.7	45
54.7	90	45
125.3	90	45
180	35.3	45
180	144.7	45
234.7	90	45
305.3	90	45
0	35.3	45
0	144.7	45

B components

φ1	Φ	φ2
0	125.3	45
0	54.7	45
60	125.3	45
60	54.7	45
120	125.3	45
120	54.7	45
180	125.3	45
180	54.7	45
240	125.3	45
240	54.7	45
300	125.3	45
300	54.7	45
0	125.3	45
0	54.7	45

C components

φ1	Φ	φ2
90	45	0
90	135	0
270	45	0
270	135	0
0	90	45
180	90	45

Rotated cube

φ1	Φ	φ2
315	0	0
45	0	0
225	0	0
135	0	0
45	180	0
315	180	0
135	180	0
225	90	0
45	90	0
315	90	0
135	90	0
225	90	0
315	90	90
135	90	90
225	90	90
45	90	90